Activities Report 2021

Reference: SFRH/BD/146886/2019

January 31, 2022

The present activities report regards the work developed by the research fellow João Miguel Peixoto Oliveira for the research grant SFRH/BD/146886/2019, under the guidance of Bernardo Gonçalves Almeida and Leonard Deepak Francis. The work plan consists of studying multiferroic bilayer composites for coupled magnetic-electric-optical functionalization.

1 Introduction

Multiferroics magnetoelectric strain coupled ferroelectric-ferromagnetic nanocomposite systems allow the magnetic (electric) control of the electric polarization (magnetization). These static magnetoelectric effects permit the current-free ability to read and write a magnetic state by an electric voltage as well as multiple functionalities in a single structure. However, beyond static magnetic-electric coupling, dynamic or optical magnetoelectric effects have been poorly explored and are equally interesting. They allow the non-contact manipulation of magnetic/electric responses, the strain control of electro-optic effects or the direct magnetic detection/manipulation by an optical signal vastly widening the composite functionalities. As such, this work envisages a coherent study of bilayer magnetoelectric nanostructures composed of magnetostrictive (Co,Ni)Fe_2O_4 and ferroelectric (Li,K)NbO_3 or $LiTaO_3$. These are commonly used in waveguide and integrated optics applications. Their use within magnetoelectric bilayer systems then allows deepening the understanding of dynamic magnetoelectric effects, while attaining new coupled optical-electric-magnetic multifunctionalities.

The objectives proposed for the research grant are:

1. Synthesis of laser-ablated (10 nm to 200 nm thin films composed by epitaxial piezoelectric/magnetostrictive bilayers with different optimized layer thicknesses. Systematic characterization of their structural, chemical, and morphological properties. Of relevance is to study and tailor layer/layer and layer/substrate interface structures towards improving the interface engineered strain coupling.
2. Systematic characterization of the magnetic properties as a function of temperature and magnetic field. Study of the type of magnetic ordering, critical temperatures, and the influence of interfacial strain. Also, attention will be paid to the determination and exploration of the magnetization behaviour near the ferroelectric layers Curie temperatures.
3. Systematic characterizations of the frequency-dependent electric properties and relaxation behaviour (impedance spectroscopy, P–-E hysteresis cycles) of the films. Determination of the influence of strain on the onset of polar order, critical temperatures, and coercive fields.
4. Studies of electric field/magnetic field induced coupled magnetic and electric responses. Determination of the magnetostrictive and piezoelectric induced

strains on the optical properties of the films (e.g., second harmonic generation, electro-optical behaviour). Characterization of the interplay between the local interfacial structure and the magnetic, electric, and optical behaviour, towards attaining new coupled optical-electric-magnetic multifunctionaliszed nanocomposites.

2 Work Plan Progress

The work began with the $CoFe_2O_4/LiNbO_3$ samples on platinum-coated silicon substrates (Si/Pt). One of the main foci of the work plan, the impedance spectroscopy measurements were hindered on most samples of these samples because they would tend to short-circuit. The likely cause of the short-circuits were the pinholes on the thin films visible on scanning electron micrographs, formed due to degradation of the platinum electrode layer of the substrate under the high deposition temperatures needed for the films. As such, during 2021 the bilayer films have been deposited in different substrates to characterize growth conditions, improve their structural/morphological quality, and promote film orientation. Additionally, barium titanate ($BaTiO_3$, BTO) was also explored as an additional ferroelectric layer, for these composite films. Their structural, morphological, and spectroscopic properties were characterized. The dielectric properties were measured by impedance spectroscopy. They were modelled in or to determine relaxation processes, activation energies, conductivity mechanisms and bilayer coupling behaviour.

3 Deposition Conditions

Thin-film samples of the magnetostrictive $CoFe_2O_4$ (CFO) and the ferroelectrics $LiNbO_3$ (LNO) and $BaTiO_3$ (BTO) were produced by laser ablation on substrates of:

- platinum-coated silicon ($Si/SiO_2/TiO_2/Pt$), shortened to SiPt;
- Si;
- Highly conductive Si, formed by As doping on Si (Si:As), referred to as Sn;
- $SrTiO_3(100)$;
- Conductive $SrTiO_3(100)$ due to high doping with Nb ($SrTiO_3$:Nb), referred to as STOn;
- fluorine-doped tin oxide (FTO) coated glass slides.

The Si and $SrTiO_3$substrates were used to characterize the structure, morphology, and spectroscopic properties of the samples. Since Si and $SrTiO_3$substrates are not conductive enough for electric measurements, their similar conductive Sn and STOn substrates were used for impedance spectroscopy. With this, the substrate acts as a bottom electrode for the measurements.

The work in 2021 was mostly focused on bilayer thin films of $CoFe_2O_4/BaTiO_3$. The produced samples vary mainly by the substrate used and the deposition time (layer thickness) of the barium titanate layer.

First, a set of pulsed laser deposition conditions deemed adequate for film deposition were found for each target and are displayed in Table 1.

Table 1: Laser deposition conditions used for each target. The controllable variables in the deposition setup were the work gas atmospheric pressure (P), the laser energy (E) and pulse frequency (f), the distance between the target and substrate (d), and the temperature of the substrate (T).

Film	P (mbar)	E (mJ)	f (Hz)	d (cm)	T (°C)
$CoFe_2O_4$	0.1	350	10	3.5	650
$LiNbO_3$	0.1	350	6	4.0	650
$BaTiO_3$	0.03	400	5	5.0	700

Subsequent samples were produced following these deposition conditions and the list is displayed from Tables 2 to 6. Each of these tables corresponds to one thin-film system.

Table 2: Deposition conditions of the $CoFe_2O_4$ samples. The remaining preparation conditions are shown in Table 1.

Sample	Substrate	Film	d (cm)	Time (min)
STO–CFO 01	$SrTiO_3$	$CoFe_2O_4$	5.0	30
STO–CFO 02	$SrTiO_3$	$CoFe_2O_4$	3.5	40
STOn–CFO 02	$SrTiO_3$:Nb	$CoFe_2O_4$	3.5	40
SP–CFO 02	SiPt	$CoFe_2O_4$	3.5	40
SP–CFO 03	SiPt	$CoFe_2O_4$	3.5	15
SP–CFO 04	SiPt	$CoFe_2O_4$	3.5	30
Sn–CFO 01	Si:As	$CoFe_2O_4$	3.5	40
Sn–CFO 02	Si:As	$CoFe_2O_4$	3.5	60

Table 3: Deposition conditions of the $BaTiO_3$ samples. The remaining preparation conditions are shown in Table 1.

Sample	Substrate	Film	multicolumn1cTime (min)	T (°C)
SP–BTO 01	SiPt	$BaTiO_3$	30	700
SP–BTO 02	SiPt	$BaTiO_3$	15	700
SP–BTO 03	SiPt	$BaTiO_3$	45	700
SP–BTO 04	SiPt	$BaTiO_3$	5	700
SP–BTO 05	SiPt	$BaTiO_3$	2	700
SP–BTO 06	SiPt	$BaTiO_3$	30	650
Sn–BTO 01	Si:As	$BaTiO_3$	15	700
Sn–BTO 02	Si:As	$BaTiO_3$	30	700
Sn–BTO 03	Si:As	$BaTiO_3$	45	700

Table 4: Deposition conditions of the bilayers $CoFe_2O_4/BaTiO_3$ samples. The remaining preparation conditions are shown in Table 1.

Sample	Substrate	Film	Time (min)	T (°C)
SP–CFOBTO 01	SiPt	$CoFe_2O_4/BaTiO_3$	30/30	650/700
SP-CFOBTO 02	SiPt	$CoFe_2O_4/BaTiO_3$	40/2	650/700
SP-CFOBTO 03	SiPt	$CoFe_2O_4/BaTiO_3$	40/5	650/700
SP-CFOBTO 04	SiPt	$CoFe_2O_4/BaTiO_3$	40/15	650/700
SP-CFOBTO 05	SiPt	$CoFe_2O_4/BaTiO_3$	40/30	650/700
Sn–CFOBTO 01	Si:As	$CoFe_2O_4/BaTiO_3$	40/15	650/700
Sn-CFOBTO 02	Si:As	$CoFe_2O_4/BaTiO_3$	40/30	650/700
Sn–CFOBTO 03	Si:As	$CoFe_2O_4/BaTiO_3$	40/45	650/700
Sn–CFOBTO 04	Si:As	$CoFe_2O_4/BaTiO_3$	40/10	650/700
Sn–CFOBTO 05	Si:As	$CoFe_2O_4/BaTiO_3$	40/5	650/700
Sn–CFOBTO 06	Si:As	$CoFe_2O_4/BaTiO_3$	60/15	650/700
STO–CFOBTO 01	$SrTiO_3$	$CoFe_2O_4/BaTiO_3$	40/15	650/700
STOn–CFOBTO 01	$SrTiO_3$:Nb	$CoFe_2O_4/BaTiO_3$	40/15	650/700
STO–CFOBTO 02	$SrTiO_3$	$CoFe_2O_4/BaTiO_3$	40/30	650/700
STOn–CFOBTO 02	$SrTiO_3$:Nb	$CoFe_2O_4/BaTiO_3$	40/30	650/700
STO–CFOBTO 03	$SrTiO_3$	$CoFe_2O_4/BaTiO_3$	40/45	650/700
STOn–CFOBTO 03	$SrTiO_3$:Nb	$CoFe_2O_4/BaTiO_3$	40/45	650/700
FTO–CFOBTO 01	FTO	$CoFe_2O_4/BaTiO_3$	40/30	500/500

Table 5: Deposition conditions of the $LiNbO_3$ samples. The remaining preparation conditions are shown in Table 1.

Sample	Substrate	Film	P (mabar)	d (cm)	Time (min)
S–LNO 01	Si	$LiNbO_3$	0.1	4.0	45
SP–LNO 01	SiPt	$LiNbO_3$	1	3.3	45
SP–LNO 02	SiPt	$LiNbO_3$	0.1	3.3	45
SP–LNO 03	SiPt	$LiNbO_3$	0.1	4.0	5
STO–LNO 01	SrTt03	$LiNbO_3$	0.1	4.0	45

Table 6: Deposition conditions of the bilayer $CoFe_2O_4/LiNbO_3$ samples. The remaining preparation conditions are shown in Table 1.

Sample	Substrate	Film	d (cm)	Time (min)
SP–CFOLNO 01	SiPt	$CoFe_2O_4/LiNbO_3$	5.0/4.0	30/5
SP–CFOLNO 02	SiPt	$CoFe_2O_4/LiNbO_3$	3.5/4.0	40/2

4 Scanning Electron Microscopy

The morphology of the produced thin films samples was characterized by scanning electron microscopy (SEM) and their chemical composition by energy-dispersive X-ray spectroscopy (EDX). SEM micrographs of the surface give an idea of the surface morphology, while the micrographs of lateral cuts of the thin give an image of the type of growth and the thickness of the film.

Cobalt Ferrite Samples

The SP-CFO films grow polycrystalline with a rough surface on top of platinum covered silicon, as can be seen in the scanning electron micrographs of the surface of these samples in Figure 1.

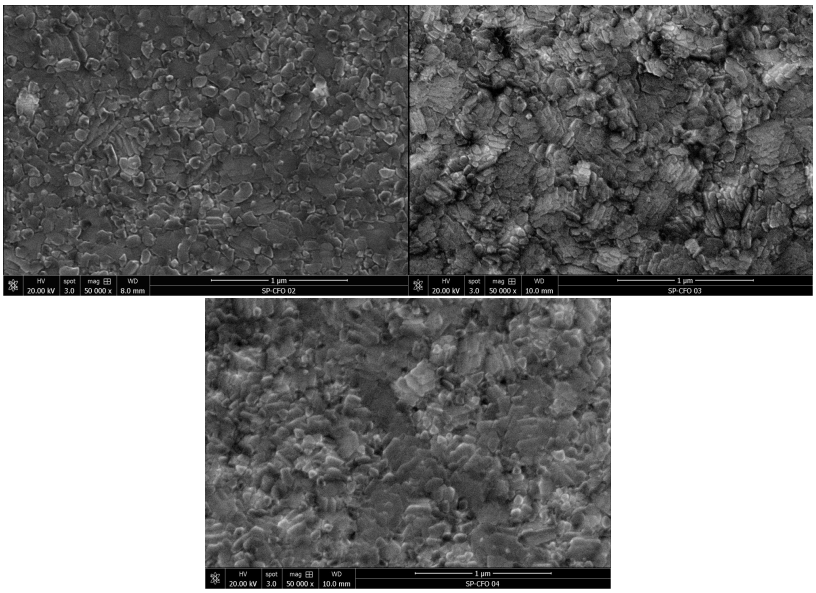

Figure 1: scanning electron micrograph of the surface of the sample SP-CFO 02, 03 and 04.

Barium Titanate Samples

SEM micrographs of the surface and lateral cuts of the samples SP-BTO 01, 02, and 03 are displayed in Figure 2. Small grains are visible on the surface of the $BaTiO_3$. These correspond to material that is agglomerating as the layer forms and its thickness progressively increases. It also indicates some degree of roughness of the surface of these films. The $BaTiO_3$ layers have columnar growth.

From the layer thickness obtained from these micrographs and assuming a linear deposition rate, the $BaTiO_3$ layer has a deposition rate around 9.3 nm/min, see Figure 3. However, the deposition rate can change between deposition due to different factors like how well centred the plume is with the substrate or the condition of the target. As such, care must be taken to control these factors during depositions.

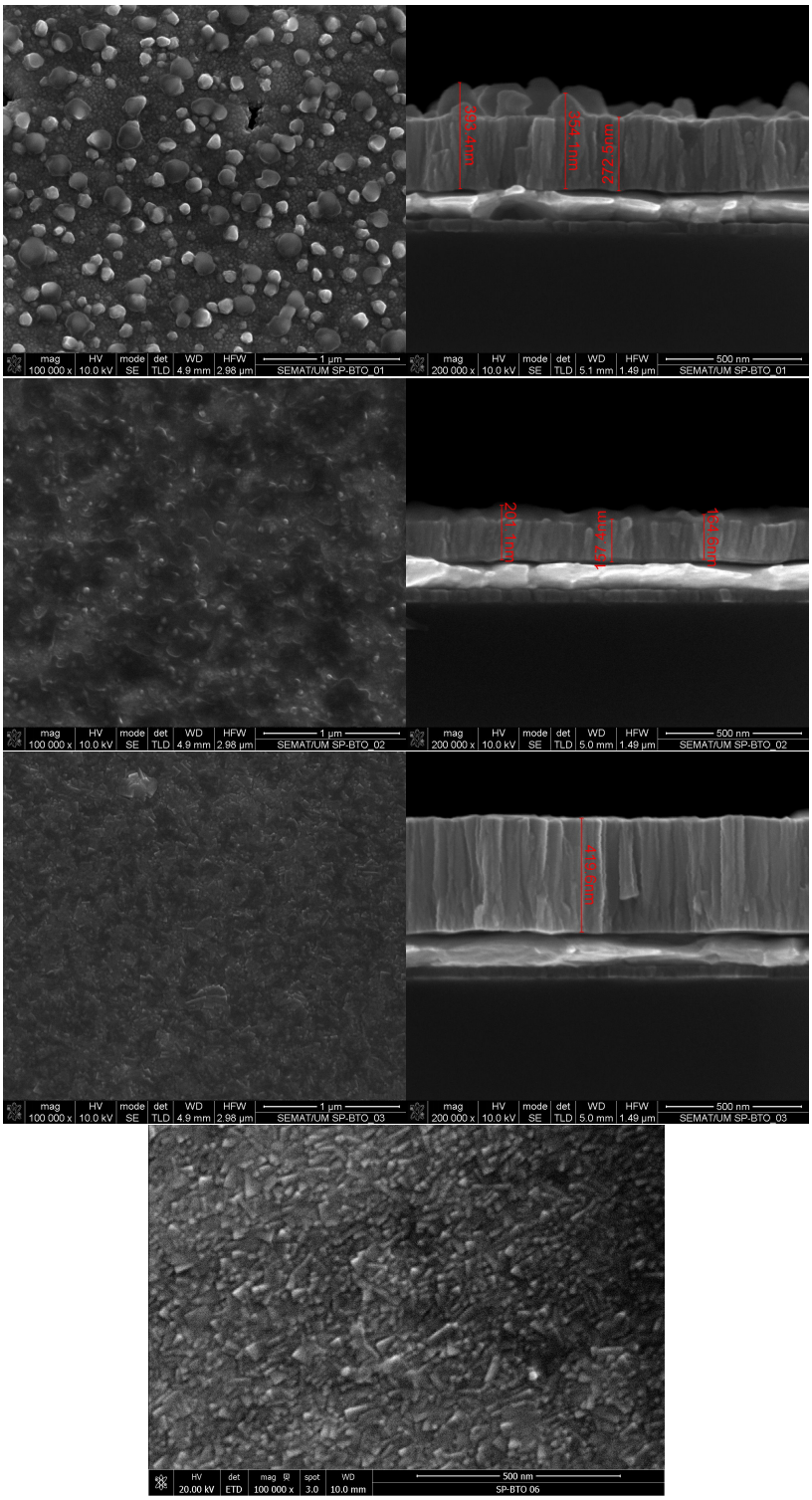

Figure 2: scanning electron micrographs of the surface and lateral cut of the sample SP-BTO 01, 02, 03, and 06. From the lateral cuts the measured thickness of the samples SP-BTO 01, 02, and 03 was 272.5 nm, 157.4 nm, and 419.6 nm, respectively.

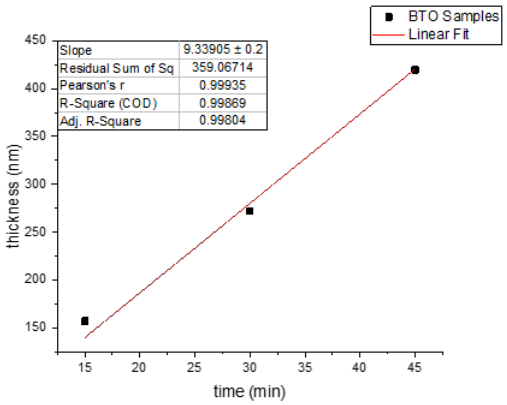

Figure 3: Thickness of the SP-BTO 01, 02, and 03 samples, determined by scanning electron microscopy, as a function of the deposition time. The linear fit that gives a deposition rate of 9.3 nm/min for the barium titanite layer.

The scanning electron micrographs of the samples SP-BTO 01, SP-BTO 02 and SP-CFOBTO 03 show pinholes on the film, exposing the platinum layer. Figure 4 is a micrograph of the sample SP-BTO 02, the surface of this sample is covered in pinholes. On the border of the lateral cut, it is visible that the pinhole is in both the barium titanite film and the platinum layer below (white layer). These pinholes make it impossible to realize dielectric measures of the films because the top electrode would short-circuit with the platinum layer that acts as a bottom electrode. The pinholes in the $Si/SiO_2/TiO_2/Pt$ substrates occurs when the substrate is heated to temperatures above 650 °C in oxygen leading to the formation of hillocks and roughening.

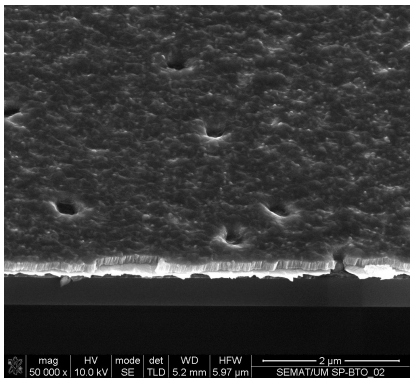

Figure 4: Pinholes visible on the film of the sample SP-BTO 02. On the border of the lateral cut, it is visible that the pinhole is in both the barium titanite film and the platinum layer below (white layer).

Cobalt Ferrite – Barium Titanate Bilayers

On the sample SP-CFOBTO 01, the $CoFe_2O_4$ layer is hard to distinguish from the layer of $BaTiO_3$, because they have similar electronic densities, giving similar shades of grey in the micrographs in Figure 5. Nevertheless, the cobalt ferrite layer appears to have a thickness of around 25 nm.

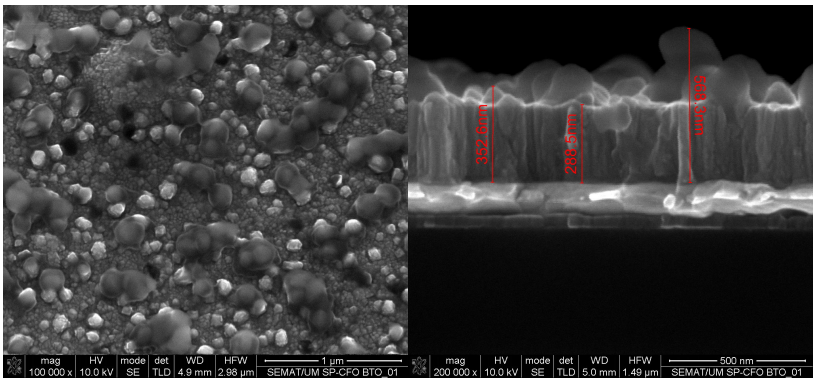

Figure 5: scanning electron micrograph of the sample SP-CFOBTO 01. The bilayer has a thickness of around 283.5 nm. With 258.5 nm for the barium titanite layer and 25 nm for the cobalt ferrite layer.

Figure 6 shows scanning electron micrographs of the samples: Sn-BTO 01, 02, 03, and 05. The deposition condition of these samples differs by the deposition time of the $BaTiO_3$ layer. On the micrographs, it is visible a difference in particle sizes. The particles on the micrograph of the sample Sn-CFOBTO 01 have a diameter of around 57 nm (assuming a circular shape), while the diameter for the sample Sn-CFOBTO 03 is around 140 nm. The higher particle sizes are observed in the thicker films, since they spend more time at high temperatures, during the preparation process, and this promotes grain growth during the deposition.

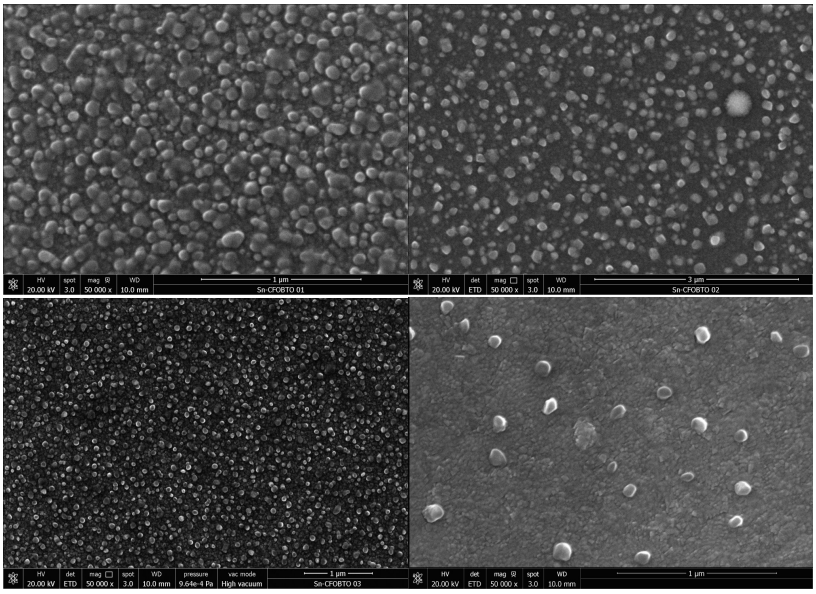

Figure 6: scanning electron micrographs of the surface of the samples Sn-CFOBTO 01, 02, 03 and 05.

Figure 7 show a scanning electron micrograph of the surface of the sample FTO-CFOBTO. From the micrograph, the film shows a polycrystalline morphology, composed of grains with random orientations, and a rough surface.

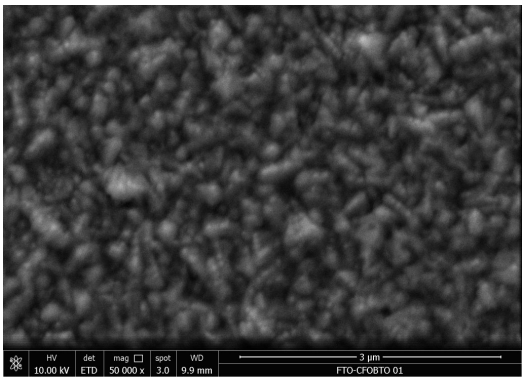

Figure 7: scanning electron micrographs of the surface of the samples FTO-CFOBTO 01.

5 X-Ray Diffraction

Cobalt Ferrite Samples

Figure 8 displays the X-ray diffractograms SP-CFO 02, 03, and 04 samples with a zoom-in of the region of 2θ between 38° to 42°. Figure 9 displays the X-ray diffractogram of the STO-CFO 01 sample with a zoom-in of the region of 2θ between 42° to 48°. The different substrates induce the cobalt ferrite layer growth with different crystallographic orientations, namely, (222) in the case of the platinum-coated substrate, and (400) on the STO substrate.

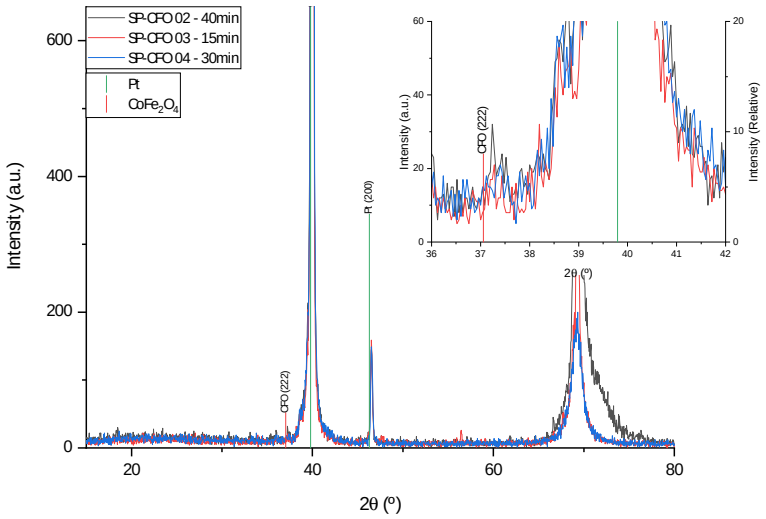

Figure 8: X-ray diffractograms of the bilayer samples SP-CFO 02, 03, and 04 with a zoom-in of the region of 2θ between 36° to 42°. In the zoom-in region is visible a $CoFe_2O_4$ (222).

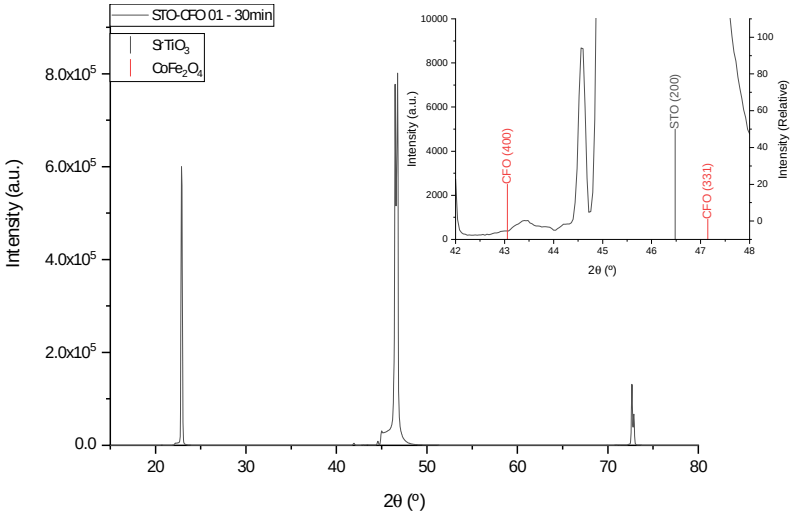

Figure 9: X-ray diffractograms of the bilayer samples STO-CFO 01 with a zoom-in of the region of 2θ between 42° to 48°. In the zoom-in region is visible a $CoFe_2O_4$ (400).

Barium Titanate Samples

Figures 10 to 11 display the X-ray diffractograms of the bilayer BTO on SP and Sn substrates with a zoom-in of the region of 2θ between 42° to 48°.

In the zoom-in region, a $BaTiO_3$ peak is visible, but it is not possible to identify if it is from the cubic phase or the ferroelectric tetragonal phase. Nevertheless, it wide indicates the superposition of the (200) and (002) peaks, indicative of the presence of the tetragonal, ferroelectric, structure of BTO. In the SP samples, the intensity of this peak increases with the deposition time, except for the sample SP-BTO 06, which can indicate that the lower temperature promotes a lower crystallisation. This peak on the Sn samples has a lower intensity than the SP sample with correspondent deposition time, and it is not visible on the SP sample with lower deposition time.

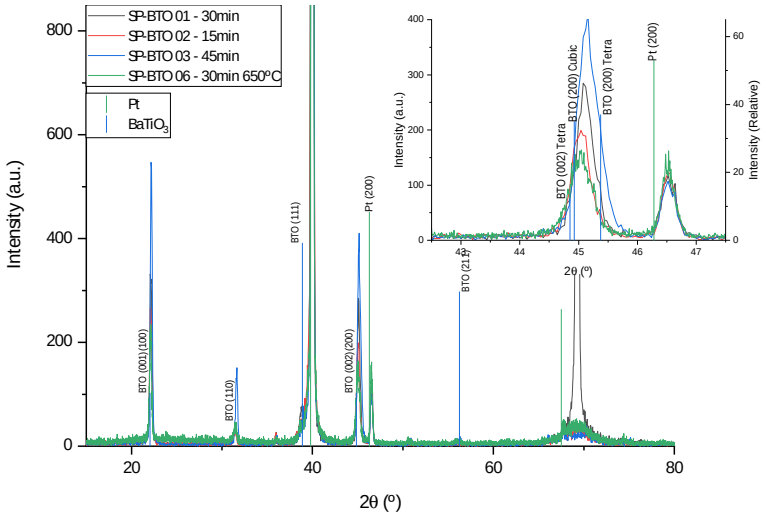

Figure 10: X-ray diffractograms of the bilayer samples SP-CFOBTO 01, 02, 03, and 06 with a zoom-in of the region of 2θ between 42° to 48°. In the zoom-in region is visible a $BaTiO_3$ peak but is not possible to identify the phase and the platinum peak (200).

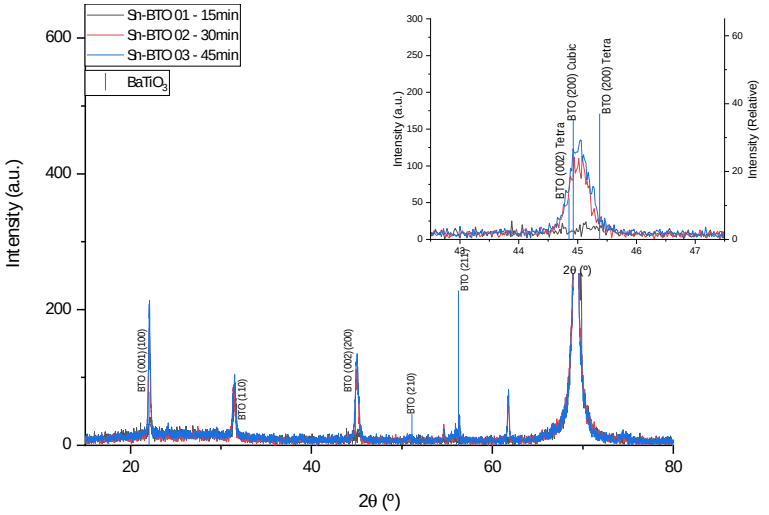

Figure 11: X-ray diffractograms of the bilayer samples Sn-CFOBTO 01, 02, and 03 with a zoom-in of the region of 2θ between 42° to 48°. In the zoom-in region is visible a $BaTiO_3$ peak but is not possible to identify the phase and the platinum peak (200).

Cobalt Ferrite – Barium Titanate Bilayers

Figures 12 to 14 display the X-ray diffractograms of the bilayer CFOBTO on the different substrates with a zoom-in of the region of 2θ between 42° to 48°. In the zoom-in region of the samples STO-CFOBTO, the substrate's $SrTiO_3$ (200) peak from the substrate and the cubic spinel $CoFe_2O_4$ (400) peak are present. Also observed are the tetragonal $BaTiO_3$ (002), and (200) peaks. In the case of the substrates SP and Sn, a $BaTiO_3$ peak is visible in this region. It is not clear if it is from the cubic phase or the ferroelectric tetragonal phase. Nevertheless, they confirm the perovskite structure of $BaTiO_3$.

The film in the STO-CFOBTO samples appears to grow more oriented than the SP and Sn substrates that are polycrystalline with peaks in more crystallographic orientations.

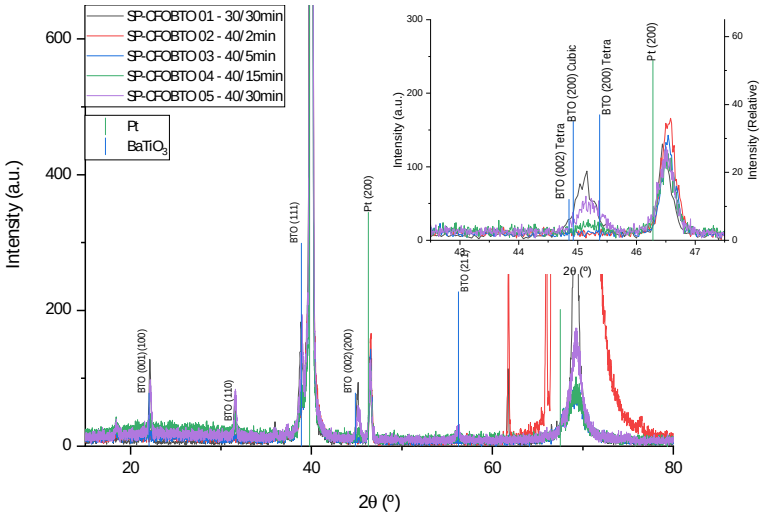

Figure 12: X-ray diffractograms of the bilayer samples SP-CFOBTO 01, 02, 03, 04, and 05 with a zoom-in of the region of 2θ between 42° to 48°. In the zoom-in region is visible a $BaTiO_3$ peak but is not possible to identify the phase and the platinum peak (200).

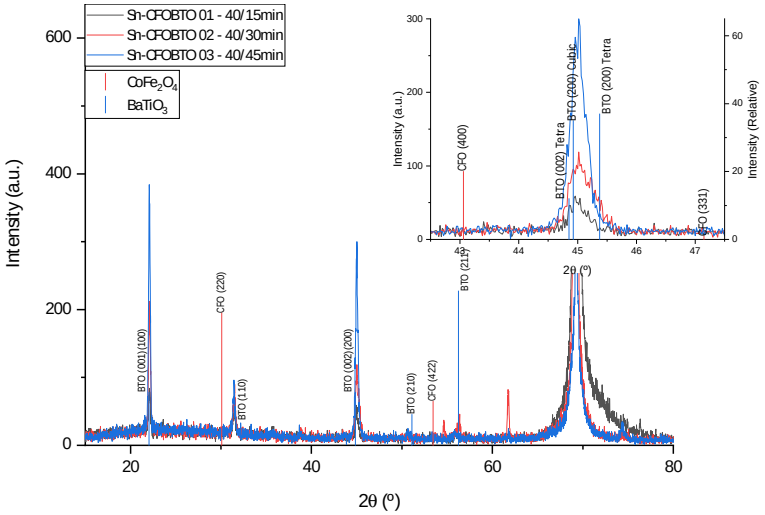

Figure 13: X-ray diffractograms of the bilayer samples Sn-CFOBTO 01, 02, and 03 with a zoom-in of the region of 2θ between 42° to 48°. In the zoom-in region is visible a $BaTiO_3$ peak but is not possible to identify the phase.

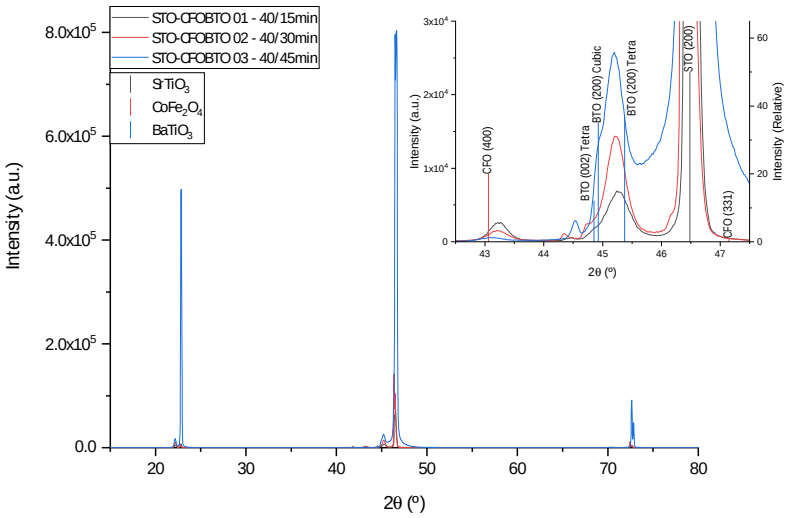

Figure 14: X-ray diffractograms of the bilayer samples STO-CFOBTO 01, 02, and 03 with a zoom-in of the region of 2θ between 42° to 48°. In the zoom-in region is visible the $SrTiO_3$ (200), $CoFe_2O_4$ (400), cubic $BaTiO_3$ (200), tetragonal $BaTiO_3$ (002), and (200).

The FTO-CFOBTO sample was deposited at 500 °C instead of the 650/700 °C used with other substrates because the glass slide has a glass transition at around 560 °C. The X-ray diffractograms of an FTO substrate and the sample FTO-CFOBTO in Figure 15 shows the presence of a polycrystalline $BaTiO_3$ film with the peaks from multiple growth directions: (100)/(001), (101), (200)/(002), (211)/(112). For the $CoFe_2O_4$ phase, the (311) peak of its cubic spinel phase is observed near 37°.

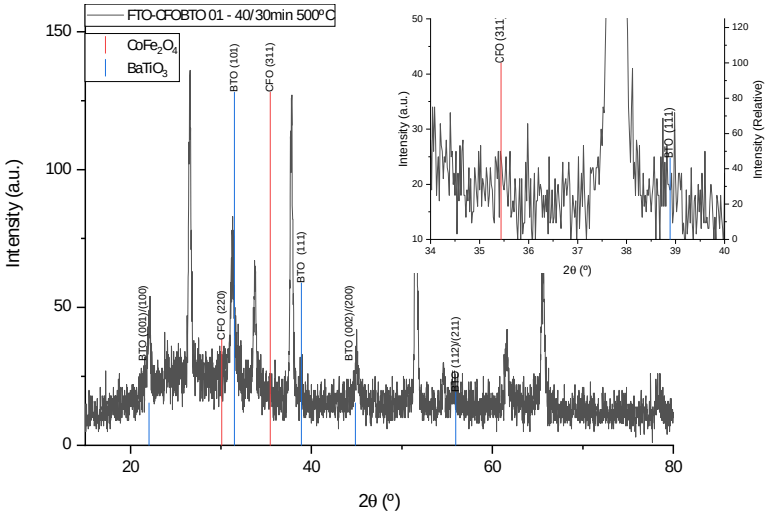

Figure 15: X-ray diffractogram of an FTO substrate and the bilayer sample FTO-CFOBTO 01 sample with a zoom-in of the region of 2θ between 34° to 40°.

6 Raman Spectroscopy

Barium titanate undergoes a phase transition around 130 °C, from the high-temperature cubic (paraelectric) phase to the tetragonal ferroelectric phase that is kept down to room temperature. In nanoscopic materials, it is hard to distinguish from X-ray diffraction alone the presence of the tetragonal phase since it corresponds to a slight distortion of the cubic phase. On the other hand, due to symmetry, the cubic phase of $BaTiO_3$ does not produce Raman vibration modes [1]. As such, Raman spectroscopy should only detect the existence of the ferroelectric tetragonal phase, unlike the X-ray diffraction that can detect both. Nevertheless, the disorder of the titanium position in the nominally cubic phase can create broad peaks centred around 260 cm^{-1} and 260 cm^{-1} [1].

[1]: Smith et al. (2008), "Crystal structure and the paraelectric-to-ferroelectric phase transition of nanoscale $BaTiO_3$"

The most prominent Raman modes for cobalt ferrite in the cubic spinel phase are:

- 210 cm^{-1} is the $T_{1g}(3)$ mode,
- 312 cm^{-1} is the E_g mode,
- 470 cm^{-1} is the $T_{1g}(2)$ mode,
- 575 cm^{-1} is the $T_{1g}(1)$ mode,
- 624 cm^{-1} is the $A_{1g}(2)$ mode,
- 695 cm^{-1} is the $A_{1g}(1)$ mode.

The Raman modes of cobalt ferrite below 600 cm^{-1} are from symmetric and anti-symmetric bending of oxygen atom in the M-O bond (M=Co,Fe) in the octahedral sublattice, while the modes above 600 cm^{-1} are due to symmetric stretching of the oxygen atom relative to the metal ion in the tetrahedral sublattice [2, 3].

[2]: Yu et al. (2002), "Cation migration and magnetic ordering in spinel $CoFe_2O_4$ powder: Micro-Raman scattering study"

[3]: Chandramohan et al. (2011), "Cation distribution and particle size effect on Raman spectrum of $CoFe_2O_4$"

The barium titanate main modes in the tetragonal phase are [4]:

- 185 cm^{-1} are the A_1(TO), E(TO), E(LO), A_1(LO) modes,
- 260 $cm^{-1}$is the A_1(TO) mode,
- 305 cm^{-1} are the B_1, E(TO+LO) modes,
- 520 cm^{-1} are the E(TO), A_1(TO) modes,
- 715 cm^{-1} are the E(LO), A_1(LO) modes.

[4]: Shiratori et al. (2007), "Raman scattering studies on nanocrystalline $BaTiO_3$ Part II—consolidated polycrystalline ceramics"

Raman spectroscopy was performed with an excitation wavelength of 532 nm, from 100 cm^{-1} to 1000 cm^{-1} on the samples SP-CFOBTO 02, 03, 04, 05, and SP-BTO 06.

Figure 16 shows the Raman spectra of the SP-CFOBTO samples with increasing deposition times of the barium titanate layer. The spectra were normalized for the cobalt ferrite $A_{1g}(1)$ mode at 695 cm^{-1}. There is an increase of intensity of the barium titanate modes at 305 cm^{-1} with increasing deposition time.

It is known that $BaTiO_3$ grains, in the ferroelectric phase, present a tetragonal (ferroelectric) core and a cubic (paraelectric shell), due to surface effects. As such, when reducing to the nanoscale the surface/volume ratio becomes important and the ferroelectric phase is more hindered. On the other hand, as the thickness increases, surface effects become less important, and the ferroelectric phase is more ordered as observed in our films. In this work, the Raman results indicate the stabilization of the ferroelectric phase of $BaTiO_3$ in all the films, with increased structural order as the thickness increases.

Figure 17 shows a comparison between the spectra of the samples SP-BTO 06 and SP-CFOBTO 05. Both samples have a layer of barium titanate with 30 min of deposition, although at different deposition temperatures, 650 °C for the sample SP-BTO 06 and 700 °C for the sample SP-CFOBTO 05. The barium titanate mode at 305 cm^{-1} appears less defined in the sample produced at a lower temperature. However, its presence in the BTO film and, particularly, in the CFOBTO bilayer indicates the stabilization of the ferroelectric phase of barium titanate in the deposited samples.

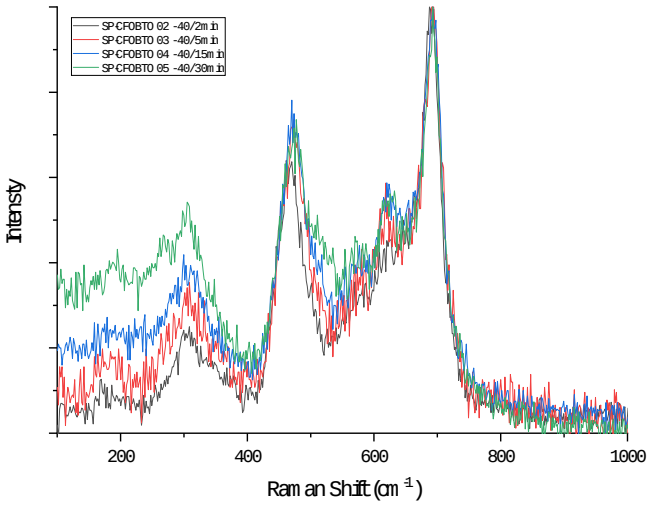

Figure 16: Raman spectra of the samples SP-CFOBTO 02, 03, 04 and 05. The spectra were normalized for the 695 cm^{-1}. The samples differ by the deposition time of the barium titanate layer.

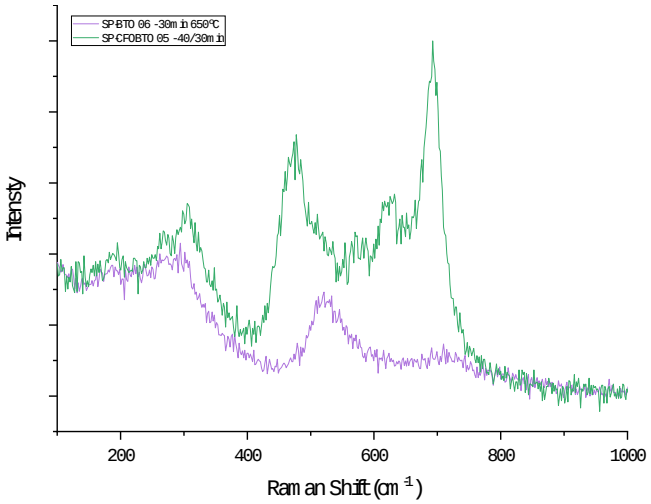

Figure 17: Raman spectra of the samples SP-BTO 06 and SP-CFOBTO 05. The spectra were normalized for the value around 100 cm^{-1} and 1000 cm^{-1}. Both samples have a layer of barium titanate with 30 min of deposition, although prepared at a different temperature, 650 °C for the sample SP-BTO 06 and 700 °C for the sample SP-CFOBTO 05.

Figure 18 and Table 7 show the result from fitting the Raman spectrum of the sample SP-CFOBTO 05, where each mode is described by a Lorentzian and the baseline is a constant. The 308.6 cm^{-1} peak is probably a combination of the E_g mode from cobalt ferrite and the B_1, E(TO+LO) modes from barium titanate.

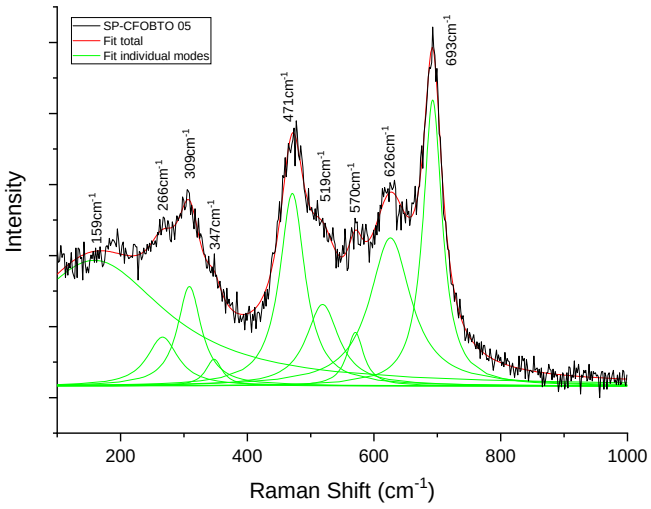

Figure 18: Raman spectrum of the sample SP-CFOBTO 05 with the obtained Lorentzian fit.

Table 7: Results obtained from the fit of the Raman spectrum of the sample SP-BTO 06.

Material	Modes	Raman Shift (cm-1)	Intensity (a.u.)	FWHM (cm-1)
–	–	347.4	0.075	31.5
$CoFe_2O_4$	$T_{1g}(2)$	471.1	0.542	48.2
$CoFe_2O_4$	$T_{1g}(1)$	570.5	0.151	32.3
$CoFe_2O_4$	$A_{1g}(2)$	625.9	0.417	78.8
$CoFe_2O_4$	$A_{1g}(1)$	692.6	0.805	36.3
$BaTiO_3$	A_1(TO), E(TO), E(LO), A_1(LO)	158.5	0.354	276.1
$BaTiO_3$	A_1(TO)	266.4	0.138	59.2
$BaTiO_3$	B_1, E(TO+LO)	308.6	0.280	45.7
$BaTiO_3$	E(TO), A_1(TO)	518.8	0.230	62.4

Figure 19 and Table 8 show the result from fitting the Raman spectrum of the sample SP-BTO 06, where each mode is described by a Lorentzian and the baseline is a constant. The 289.4 cm^{-1} peak is probably a combination of the A_1(TO), B_1, E(TO+LO). In the CFOBTO samples, this peak can be at a higher Raman shift due to the influence of the E_g mode from cobalt ferrite. The 517.5 cm^{-1} peak appears asymmetric and a second peak at 549.2 cm^{-1} was added to the fit. This asymmetry can be seen in Shiratori et al. [4].

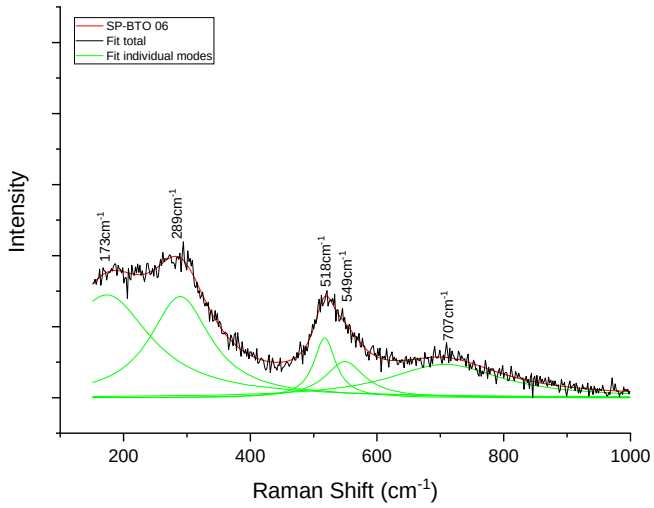

Figure 19: Raman spectrum of the sample SP-BTO 06 with the obtained Lorentzian fit.

Table 8: Results obtained from the fit of the Raman spectrum of the sample SP-CFOBTO 05.

Material	Modes	Raman Shift (cm-1)	Intensity (a.u.)	FWHM (cm-1)
$BaTiO_3$	A_1(TO), E(TO), E(LO), A_1(LO)	173.4	29.0	168.8
$BaTiO_3$	A_1(TO), B_1, E(TO+LO)	289.4	28.5	117.1
$BaTiO_3$	E(TO), A_1(TO)	517.5	16.8	42.2
$BaTiO_3$	–	549.2	10.2	75.8
$BaTiO_3$	E(LO), A_1(LO)	707.0	9.4	219.0

7 Dielectric Spectroscopy

The frequency-dependent electric properties and relaxation behaviour of the samples were studied through impedance spectroscopy. The complex electrical permittivity was obtained as a function of the temperature and frequency, with the dielectric dispersion measured from 20 Hz to 3 MHz, between room temperature and 200 °C, at every 10 °C.

Nyquist plots, with the imaginary component of electrical permittivity ϵ'' as a function of real component ϵ', display conductivity contributions and dielectric relaxations.

The conductivity contribution for the AC behaviour of the electric permittivity terms was described by:

$$\hat{\epsilon}(\omega) = i\frac{\sigma}{\omega^s \epsilon_0} \tag{1}$$

, where σ is the DC conductivity, ω is the angular frequency and ϵ_0 the vacuum permittivity. Since the permittivity depends on the inverse of the angular frequency, the conductivity contribution becomes more relevant at lower frequencies, where the $1/\omega$ term becomes elevated.

The dielectric relaxations, due to their asymmetry, were described by the Havriliak-Negami model:

$$\hat{\epsilon}(\omega) = \epsilon_\infty + \frac{\Delta\epsilon}{\left[1 + (i\omega\tau)^\alpha\right]^\beta} \tag{2}$$

, where ϵ_∞ the electrical permittivity at high frequencies, $\Delta\epsilon$ the variation in the electrical permittivity, τ the characteristic relaxation time of the medium, and α and β are empirical terms that define the asymmetry and broadness of the dispersion. The Havriliak-Negami relaxation is an empirical modification of the Debye relaxation model and reduces to it when $\alpha = 1$ and $\beta = 1$.

A sample can have multiple conductivity contributions and dielectric relaxations. For example, in the case of bilayer samples, where each layer was their contributions, and the contributions from each layer can interact with each other. As such, it was assumed that the overall permittivity of the samples results from two non-ideal capacitors in series, in the bilayer samples.

In Figure 20, it is shown the impedance spectroscopy measured for a sample of SP-CFOLNO at 80 °C. The real and imaginary components of the electrical permittivity as a function of the frequency and their Nyquist plot are represented. At lower frequencies, it is visible a reciprocal relation of the imaginary component of the electrical permittivity with the frequency and a linear component on the right side of the Nyquist plot. They are an indication that this frequency region is dominated by the conductivity term. On the other hand, and at higher frequencies, each drop of the real component of the permittivity, peak on the imaginary part, and corresponding semi-circle on the Nyquist plot comes from a dielectric relaxation.

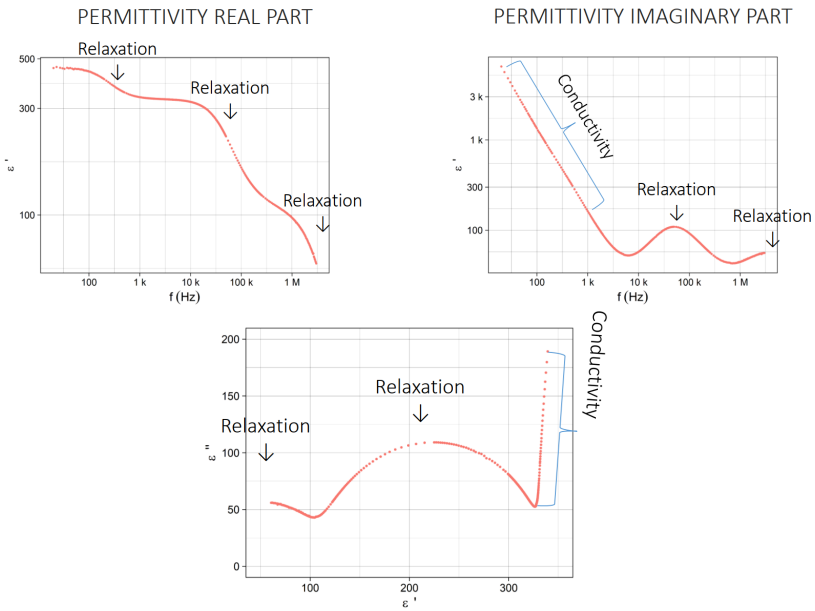

Figure 20: Example of an electric impedance measurement of an SP-CFOLNO sample ate 80 °C. a) real component ϵ' of the dielectric dispersion. b) imaginary component ϵ'' of the dielectric dispersion. c) Nyquist plot, with the imaginary component of electrical permittivity ϵ'' as a function of real component ϵ'.

Fitting the spectrum at a given temperature with these models gives the conductivities and relaxation times at each temperature. The behaviour of these conductivities and relaxation times with the temperature follows the Arrhenius Law [5]:

[5]: Nuernberg (2020), "Numerical comparison of usual Arrhenius-type equations for modeling ionic transport in solids"

$$\sigma_{DC} = \frac{\sigma_{0,DC}}{T} e^{-E_{a_{DC}}/k_b T} \tag{3}$$

$$\tau = \tau_0 e^{-E_{a_{AC}}/k_b T} \tag{4}$$

From the Arrhenius plot of the conductivities and relaxation times, it is possible to obtain the corresponding activation energies.

Sn–CFO 01

Figure 21 shows the Nyquist plots of the electrical permittivity of the sample Sn-CFO 01 at all the measured temperatures. At the higher measured temperatures, it's visible a conductivity contribution and two relaxations. The conductivity increases with the temperature and starts to dominate at the higher the temperatures. It is also displayed the resulting fits with the proposed model.

Figure 22 shows a superposition of the Nyquist plots from Figure 21 and the Arrhenius plots obtained for conductivity and relaxation obtained from the fits, from each were obtained the activation energies of 0.248 eV and 0.342 eV, respectively.

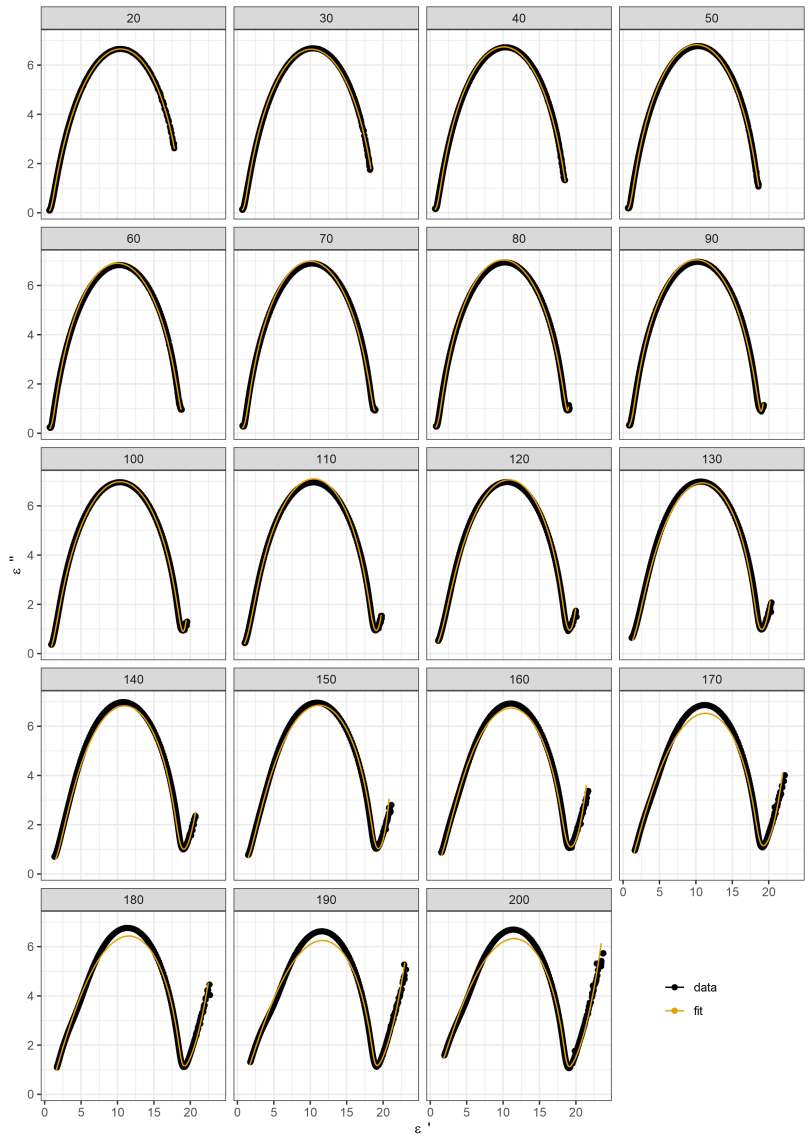

Figure 21: Nyquist plots, with the imaginary component of electrical permittivity as a function of real component, for the sample Sn-CFO 01 at different temperatures.

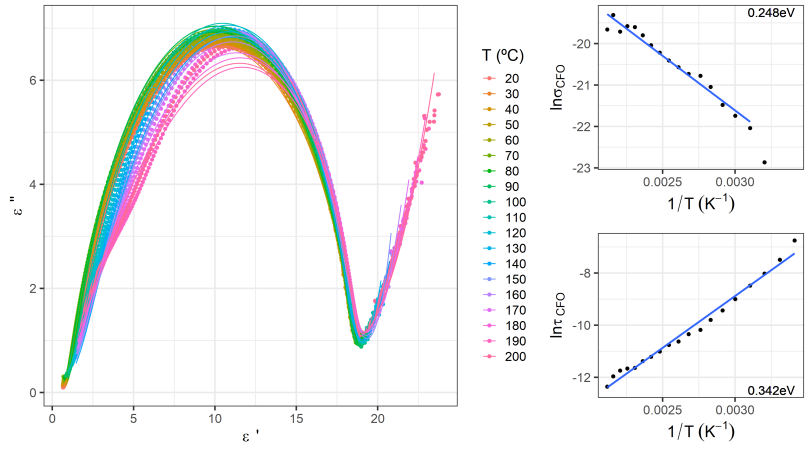

Figure 22: (left) Nyquist plot, with the imaginary component of electrical permittivity as a function of the real component, for the sample Sn-CFO 01. (right) Arrhenius plot with the DC conductivity and the characteristic relaxation time, with the activation energies determined of 0.248 eV and 0.342 eV, receptivity.

Sn–CFOBTO 01

Figure 23 shows the Nyquist plots of the electrical permittivity of the sample Sn-CFOBTO 01 at all the measured temperatures. At the higher measured temperatures, it's visible a conductivity contribution and two dielectric relaxations separate with the increase in temperature. The conductivity increases with the temperature and starts to dominate at the higher the temperatures. It is also displayed the resulting fits with the proposed model, where the left semi-circle was assigned to the $BaTiO_3$ layer and the right semi-circle to the $CoFe_2O_4$ layer.

Figure 24 shows a superposition of the Nyquist plots from Figure 23 and the Arrhenius plots obtained for conductivity and relaxation obtained from the fits, from each were obtained the activation energies of 0.069 eV and 0.320 eV, respectively, for the $BaTiO_3$ layer, and 0.291 eV and 0.080 eV, respectively, for the $CoFe_2O_4$ layer.

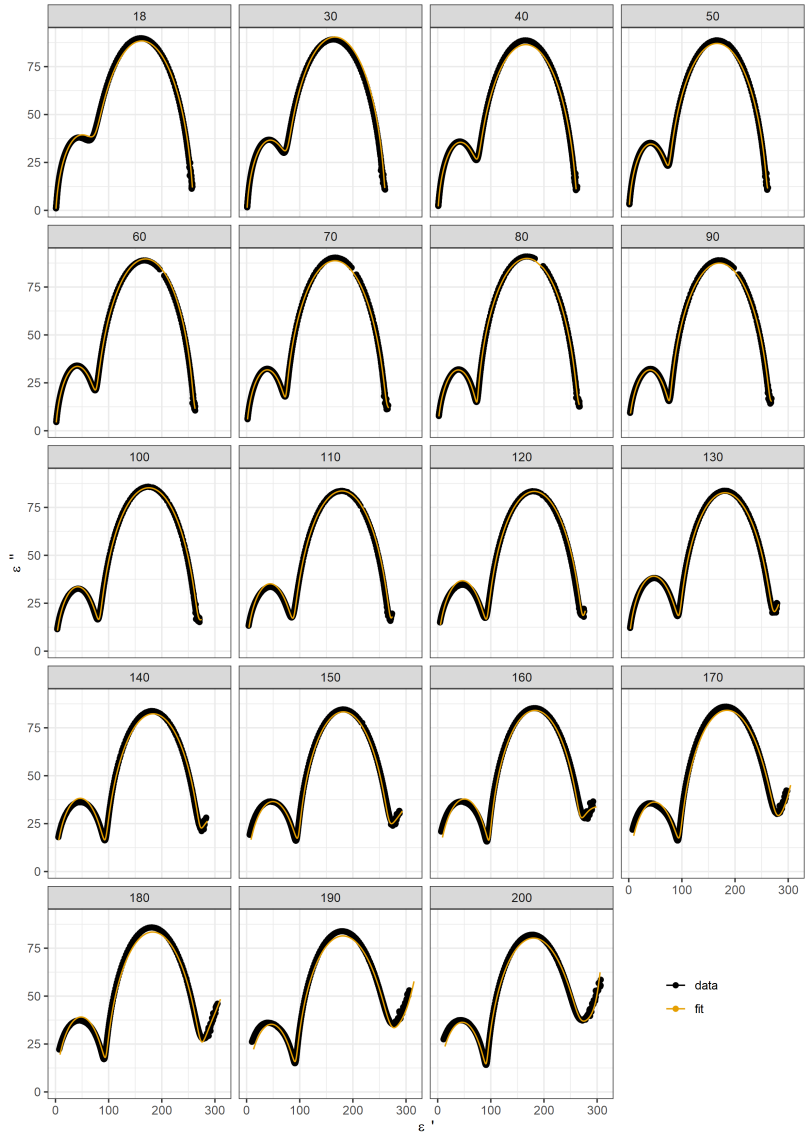

Figure 23: Nyquist plots, with the imaginary component of electrical permittivity as a function of the real component, for the sample Sn-CFOBTO 01 at different temperatures.

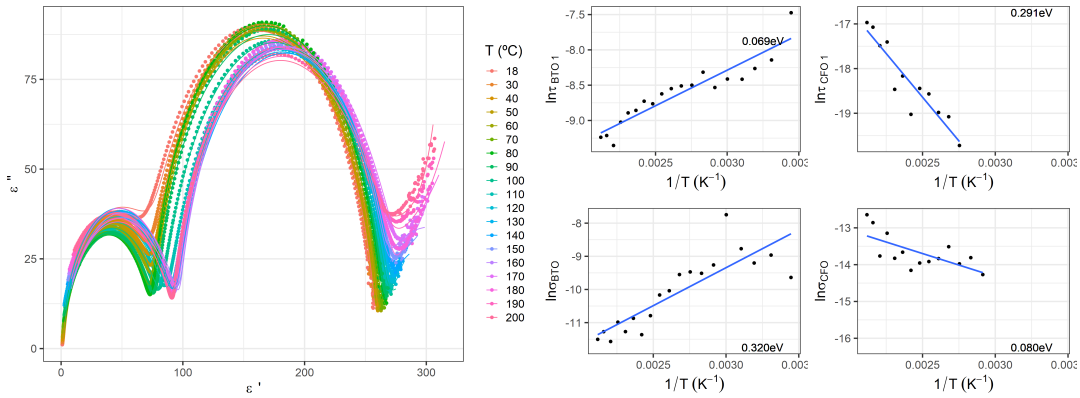

Figure 24: (left) Nyquist plot, with the imaginary component of electrical permittivity as a function of the real component, for the sample Sn-CFOBTO 01. (right) Arrhenius plot with the DC conductivity and the characteristic relaxation time, with the activation energies determined of 0.069 eV and 0.320 eV, for the $BaTiO_3$, and 0.291 eV and 0.080 eV of the $CoFe_2O_4$.

8 Work Plan

Regarding the $CoFe_2O_4/BaTiO_3$ system, the projected work remaining is mostly complete. A few more samples will be made to compare the effect of varying the thickness of both layers and the type of substrate. The characterization of the magnetic properties and second-harmonic generation measures is going to be carried out. After the $CoFe_2O_4/BaTiO_3$ system is complete, the same procedures will be carried out to study the remaining systems, namely $CoFe_2O_4/LiNbO_3$, and $CoFe_2O_4/LiTaO_3$.

9 Presentation of Results

The results for the SiPtCFOLNO samples from 2020 were presented in a poster with the title "Dielectric Properties of $CoFe_2O_4/LiNbO_3$ Bilayers" on Nanotech France 2021 from 23rd to 25th of June 2021. And, on DCE21-4th Doctoral Congress in Engineering was held on the 28th and 29th of June 2021. And, on the "MAP-Fis Research Conference" held on 9th of July 2021.

The results for the Sn-CFOBTO samples from 2021 were submitted for presentation on Nanotech France 2022 and ISAF-PFM-ECAPD 2022 with the title "Structural and dielectric properties of $CoFe_2O_4/BaTiO_3$ Bilayers deposited over highly doped Si(001) substrates".

Braga, 31st of January 2022

João Oliveira

Bibliography

[1] Millicent B. Smith et al. “Crystal structure and the paraelectric-to-ferroelectric phase transition of nanoscale $BaTiO_3$.” In: Journal of the American Chemical Society 130.22 (2008), pp. 6955–6963. DOI: 10.1021/ja0758436 (cited on page 13).

[2] T. Yu et al. “Cation migration and magnetic ordering in spinel $CoFe_2O_4$ powder: Micro-Raman scattering study.” In: Journal of Physics Condensed Matter 14.37 (2002). DOI: 10.1088/0953-8984/14/37/101 (cited on page 13).

[3] P. Chandramohan et al. “Cation distribution and particle size effect on Raman spectrum of $CoFe_2O_4$.” In: Journal of Solid State Chemistry 184.1 (2011), pp. 89–96. DOI: 10.1016/j.jssc.2010.10.019 (cited on page 13).

[4] Y Shiratori et al. “Raman scattering studies on nanocrystalline $BaTiO_3$ Part II—consolidated polycrystalline ceramics.” In: Journal of Raman Spectroscopy: An International Journal for Original Work in all Aspects of Raman Spectroscopy, Including Higher Order Processes, and also Brillouin and Rayleigh Scattering 38.10 (2007), pp. 1300–1306 (cited on pages 13, 16).

[5] Rafael Bianchini Nuernberg. “Numerical comparison of usual Arrhenius-type equations for modeling ionic transport in solids.” In: Ionics 26.5 (2020), pp. 2405–2412. DOI: 10.1007/s11581-019-03243-7 (cited on page 18).